Angle dependence of the ferromagnetic resonance linewidth and two magnon losses in pulsed laser deposited films of yttrium iron garnet, MnZn ferrite, and NiZn ferrite

Anuj K. Srivastava,[a] Michael J. Hurben, Michael A. Wittenauer, Pavel Kabos, and Carl E. Patton
Department of Physics, Colorado State University, Fort Collins, Colorado 80523

R. Ramesh
Department of Materials Engineering, University of Maryland at College Park, College Park, Maryland 20742

Paul C. Dorsey and Douglas B. Chrisey
Naval Research Laboratory, Washington, DC 20375

(Received 2 December 1998; accepted for publication 20 January 1999)

Shorted waveguide ferromagnetic resonance (FMR) measurements were made at 9.5 GHz for pulsed laser deposited yttrium iron garnet (YIG), MnZn ferrite, and NiZn ferrite films with thicknesses of 1.8, 0.5, and 1.5 μm, respectively. The FMR field versus the field angle confirmed the operational assumption of a uniform mode response. For the YIG, the linewidth was 10 Oe when the external field and magnetization vectors were perpendicular to the disk (perpendicular FMR) and increased smoothly to a maximum value of 27 Oe when the field and magnetization were in the film plane (parallel FMR). For the MnZn, the linewidth was 49 Oe at perpendicular FMR, increased with the angle between the film normal and the external field to a broad maximum of 80 Oe at 35°, and then dropped to 65 Oe at parallel FMR. For the NiZn, the linewidth was 310 Oe at perpendicular FMR, increased with the field angle to a broad maximum of 1530 Oe at 45°, and then dropped to 960 Oe at parallel FMR. The linewidths were larger than predicted for reasonable values of the Landau–Lifshitz damping and showed angle dependences which indicated nonintrinsic contributions to the loss. Two magnon scattering was used to model these linewidth differences. The angle dependences of the excess linewidths show qualitative agreement with the two magnon predictions, with inhomogeneity sizes in the submicron range and volume fractions below 1%. © *1999 American Institute of Physics.* [S0021-8979(99)00609-X]

I. INTRODUCTION

It has been demonstrated that the pulsed laser deposition (PLD) technique[1,2] can be used to fabricate epitaxial ferrite films for planar microwave devices.[3] However, one critical problem with such films is that the ferromagnetic resonance (FMR) linewidth of the samples is typically much larger than expected for single crystals.[4–7] This indicates that PLD ferrite films contain microstructural defects or impurities which increase the linewidth. Work by Dorsey *et al.*[8] indicates that the broad linewidths in PLD ferrite films are related to microstructure. These authors found that yttrium iron garnet (YIG) films grown by PLD methods showed micron sized pores which decreased in size and number as the oxygen partial pressure was reduced or the substrate temperature was increased. These changes were accompanied by a decrease in FMR linewidth.

The connection between FMR linewidth and microstructure in ferrites has received considerable attention, starting with the early work on YIG sphere surface polish by Buffler.[9] Reference 9 demonstrated that coupling between the FMR or uniform mode and degenerate spin waves leads to an increase in the measured linewidth. The theoretical basis for this ''two magnon'' linewidth may be found in the seminal paper on magnetization dynamics by Callen[10] and the formal theory of two magnon scattering by Sparks, Loudon, and Kittel.[11] Experimental and theoretical considerations for two magnon scattering are reviewed in Ref. 12. Based on these early foundations, a number of experimental studies of FMR linewidth in thin films have established strong connections between inhomogeneities, two magnon scattering, and linewidth. These included FMR measurements on Ni–Fe thin films[13–16] and work on hexagonal ferrite thin disks.[17] Reference 17 demonstrates that one can use the dependence of the FMR linewidth on the angle between the film normal and the static magnetic field to obtain qualitative and quantitative information on the film microstructure. The detailed procedure for such analyses is contained in a recent theory by Hurben and Patton.[18]

The purpose of this work was to extend the angle FMR studies cited above to PLD ferrite films. The dependence of the FMR field and linewidth on the angle between the external field and the film normal was examined for PLD films of YIG, MnZn ferrite, and NiZn ferrite. All measurements were made at 9.5 GHz by a shorted waveguide technique. The thickness of the films ranged from 0.5 to 1.25 μm. The mea-

[a]Electronic mail: anujs@lamar.colostate.edu

 © 1999 American Institute of Physics

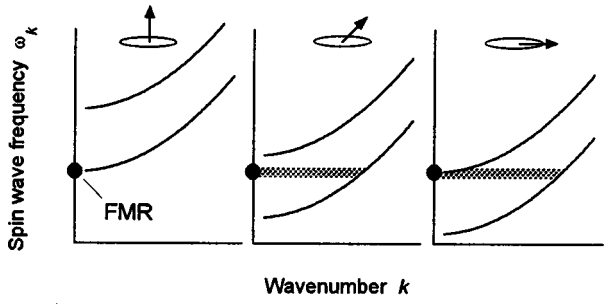

FIG. 1. Three schematic bulk spin wave dispersion curves of spin wave frequency ω_k vs wave number k for an isotropic thin film and three orientations of the external static field, as indicated. The external field has been adjusted in each diagram to obtain FMR at a common frequency indicated by the solid circle labeled FMR. The upper and lower curves in each diagram designate spin waves propagating perpendicular and parallel to the static internal field direction, respectively. The region between the two curves represents the range of available spin waves. In (b) and (c), the narrow band of spin wave modes which is degenerate with the FMR frequency is indicated by the shaded region.

sured FMR field versus angle for all the films was consistent with a uniform mode FMR model. The measured FMR linewidth versus angle revealed the presence of a microstructure based two magnon contribution to the microwave loss. The two magnon scattering model was applied to the linewidth data. The assumption of submicron size inhomogeneities with volume fractions below about 1% yielded qualitative but not quantitative fits to the data.

Section II introduces the two magnon scattering concept and establishes the connection between two magnon loss and FMR measurements at different field angles. The PLD ferrite film samples and the experimental setup are described in Sec. III. Section IV provides the operating equations for the uniform mode FMR analysis and the calculation of two magnon linewidths. Section V presents the results on (i) FMR position versus angle, and (ii) linewidth versus angle for the three PLD film materials.

II. ''ANGLE FMR'' AND TWO MAGNON LINEWIDTH

The term ''Angle FMR'' will be used to denote a series of thin film FMR experiments which are carried out at fixed frequency for different static external field directions. That is, the angle between the external field and the direction perpendicular to the film is varied between 0° and 90°, and the magnitude of the field is changed to obtain the FMR absorption peak. Under such conditions, there is also a shift in the nominal position of the spin wave band with the field angle. This shift causes a variation in the number and character of the spin wave modes which are degenerate with the FMR pump frequency. This variation in the degenerate states is the origin of the variation in the two magnon linewidth with field angle. This section provides a qualitative overview of these effects.

Figure 1 shows three schematic spin wave band diagrams of spin wave frequency ω_k versus wave number k for an isotropic magnetic thin film. The upper and lower curves in each diagram designate the bounds of the spin wave band obtained for spin waves with wave vectors which are perpendicular and parallel to the internal static field, respectively. The solid circle which decorates the spin wave frequency axis indicates the chosen FMR frequency. The specific band diagrams in (a), (b), and (c) are for perpendicular-to-film, intermediate, and in-plane field directions, respectively. These configurations are also indicated by the disk/arrow symbols for each diagram. The narrow horizontal shaded strip which extends across the spin wave band at the FMR frequency in each diagram indicates the range of spin wave states which are degenerate with the FMR frequency.

The vertical axis frequency scale is typically in gigahertz and the horizontal axis wave number scale is typically out to 5×10^5 rad/cm or so. The corresponding spin wave length is on the order of 0.1 μm, the same as the typical scale of the microstructure in PLD films. This match will be of quantitative importance for the two magnon analysis.

The effect of the field angle on the degenerate states is clear from the diagrams. When the external static field is perpendicular to the film plane, as in (a), the FMR frequency is coincident with the very bottom of the spin wave band. For this configuration, which will be termed ''perpendicular FMR,'' there are no spin wave states degenerate with the FMR frequency. The FMR linewidth observed in this configuration would be expected to contain no two magnon contribution and would be due to other processes. For the purposes of this article, relaxation processes other than two magnon processes will be termed ''intrinsic'' and described in terms of a phenomenological Landau–Lifshitz relaxation rate parameter. Diagrams (b) and (c) show that as the field orientation is changed away from perpendicular, the spin wave band shifts down and there is a smooth increase in the number of states degenerate with the uniform mode. In the limiting case of (c) with the static external field in plane, which will be termed ''parallel FMR,'' the uniform mode coincides with the top of the spin wave band in the $k=0$ limit and the number of degenerate states is maximum.

Relaxation due to the two magnon process is connected directly to the availability of degenerate states at the excitation frequency. The term ''two magnon scattering'' derives from the scenario in which a uniform mode magnon at $k=0$ scatters into a degenerate spin wave state at nonzero k. The scattering may be due to pits, pores, second phase grains, or some other microstructure related magnetic property of the material. The details of the scattering calculation are given in the references cited above.

Figure 2 illustrates the angle dependences of the linewidth effects which result from the two magnon process in thin film FMR. Figure 2 shows two curves of linewidth as a function of the angle between the film perpendicular and the static external field. The dashed line labeled INT shows the linewidth one would expect if only intrinsic processes described by Landau–Lifshitz damping were operative. The solid line, labeled INT+TM, shows the combined linewidth for both intrinsic and two magnon losses.

The results in Fig. 2 are actual computed results, based on FMR at a fixed frequency of 10 GHz for a 1-μm-thick YIG film, an intrinsic Landau–Lifshitz (LL) relaxation rate λ of 4×10^6 rad/s, scattering from spherical pores with a diameter of 0.2 μm and a volume fraction of 0.1%. The details of the two magnon analysis will be given in Sec. IV. The main

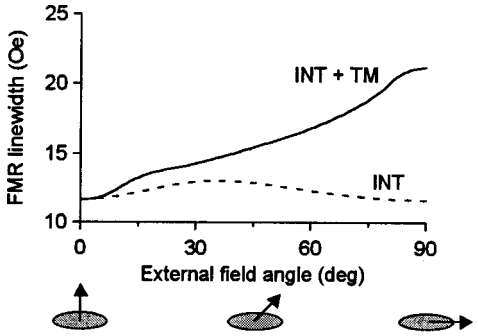

FIG. 2. Illustrative curves of the calculated ferromagnetic resonance field swept linewidth as a function of the external field angle for a typical PLD YIG film. For a given angle, the value of the field was adjusted to maintain the FMR frequency at 10 GHz. The dashed curve labeled INT shows the expected linewidth vs angle for intrinsic losses only in the form obtained from LL damping. The solid curve labeled INT+TM shows the linewidth when both two magnon losses and LL damping are included. The curves were obtained for a LL relaxation rate of 4×10^6 rad/s, spherical pores with a diameter of 0.2 μm, and a pore volume fraction of 0.1%.

point of Fig. 2 for this discussion is to demonstrate the two magnon effect in the angle FMR experiment.

Consider the intrinsic (INT) linewidth first. Even though the dashed curve is calculated for a constant value of the LL relaxation rate, the computed linewidth is still angle dependent. One does obtain the same linewidth value in the perpendicular and parallel FMR limits, but there is still a definite peak at a field angle of about 30°–40°. This peak is due to the fact that the frequency is held fixed and the field is varied to obtain the FMR response. For field angles other than 0° or 90°, the magnetization vector is out of plane and rotates as the field is changed. This rotation modifies the FMR response and gives a ''false'' peak in linewidth which is not related to loss mechanisms but to the rotation geometry.

Turn now to the solid curve. The clear rise in linewidth above the intrinsic contribution as one moves from perpendicular to parallel is due to two magnon scattering. It is related to the growth in the available number of degenerate states depicted in Fig. 1. There are essentially no such states in perpendicular FMR, while these states reach a maximum for parallel FMR.

III. EXPERIMENT

A. Samples

The FMR measurements were made for three types of PLD films, a YIG film,[19] a MnZn spinel ferrite film,[6] and a NiZn spinel ferrite film. The YIG film was deposited on a [111] gallium gadolinium garnet substrate. The substrate temperature was 600 °C and the oxygen partial pressure was 200 mTorr. The film had a nominal thickness of 1.8 μm. The spinel ferrite films were deposited on [100] MgO substrates at the Naval Research Laboratory, Washington, DC. The MnZn and NiZn compositions were deposited at 600 °C and 30 mTorr, and at 750 °C and 50 mTorr, respectively. The nominal compositions and thicknesses of the MnZn and the NiZn films were $Mn_{0.4}Zn_{0.6}Fe_2O_4$ and $Ni_{0.6}Zn_{0.4}Fe_2O_4$, 0.5 and 1.5 μm, respectively.

The films were examined optically and were found to be dense and with no obvious holes, pinholes, or large pores. Disk samples for the FMR measurements were cut from the as grown films. YIG, MnZn, and NiZn disks with diameters of 1.25, 1.5, and 1.9 mm, respectively, were produced. The edges were carefully polished to avoid spurious FMR structure.

Two magnetic parameters will be important for the FMR analysis, the magnetic induction $4\pi M_s$ and demagnetizing factor perpendicular to the disk plane N_z. A vibrating sample magnetometer (VSM) was used to measure $4\pi M_s$ on the specific disk samples used for the FMR measurements. The demagnetization factor N_z was calculated by the Osborn method.[20] The $4\pi M_s$ and N_z values for the YIG, MnZn, and NiZn samples were 2.21, 3.72, and 6.25 kG, and 0.998, 0.999, and 0.998, respectively.

Magnetic anisotropy is often an important consideration in ferromagnetic resonance experiments. The nominal cubic magnetocrystalline anisotropy for the materials listed above is small compared to the shape anisotropy for the thin film geometry. For the cubic materials of interest here, the effective anisotropy fields, for example, are in the 40–100 Oe range.[21,22] The effective shape anisotropy dominates these cubic effects. The two magnon analysis used here will not consider cubic anisotropy effects.

Thin films may also have growth related anisotropies. Typically, one may have a uniaxial or planar anisotropy due to film substrate thermal expansion mismatch, lattice mismatch, or film microstructure. The form of the free energy associated with such anisotropy is the same as the demagnetization free energy and any such anisotropy component may be folded into an effective $4\pi M_s$ value. As will be shown shortly, the FMR data yield fit $4\pi M_s$ values which are very close to the $4\pi M_s$ measured by magnetometry and indicates that any growth related anisotropy is small.

An additional materials parameter, the exchange stiffness D, is of critical importance for the two magnon analysis. As will be evident from Sec. IV B, this D parameter controls the curvature of the spin wave band. This curvature, in turn, controls the k distribution of the degenerate states which contribute to the scattering. For the two magnon linewidth evaluations in Sec. V, two values of D were used. For YIG, the D parameter was set at 5×10^{-9} Oe cm^2/rad^2, a typical room temperature value.[23] For the MnZn and NiZn materials, the D parameter was set at 7×10^{-9} Oe cm^2/rad^2. There are no reported experimental D values for MnZn or NiZn ferrite. The 7×10^{-9} Oe cm^2/rad^2 value is based on exchange stiffness measurements by Brillouin light scattering on the Li-ferrite system.[24] The measured D for Li ferrite was scaled according to the relative Curie temperatures for the Li ferrite and MnZn and NiZn ferrite systems.[21]

B. Microwave measurements

The FMR field and half-power linewidth were measured by a shorted waveguide technique.[17] The film was positioned in the waveguide to place the linearly polarized microwave field in the film plane. The static magnetic field was applied

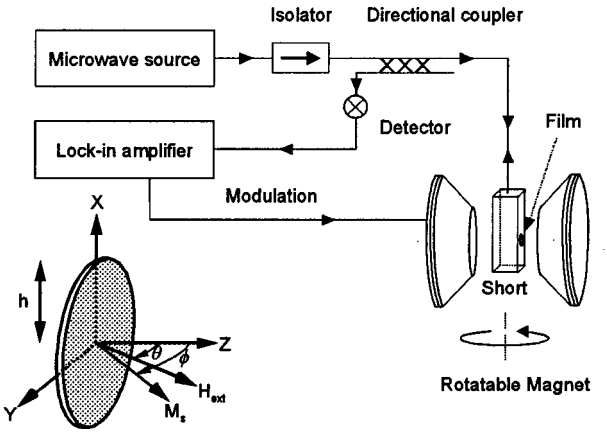

FIG. 3. Schematic diagram of the 9.5 GHz shorted waveguide spectrometer used for the FMR field and linewidth measurements vs field angle. The microwave source provides power to the film positioned in the short. Reflected power is detected and analyzed by the lock-in amplifier. The lock-in reference is used for field modulation. The magnet may be rotated to change the direction of the static field relative to the sample. The inset shows the sample and field geometry. The film is in the $X-Y$ plane. The microwave magnetic field **h** is along the X direction. The static external magnetic field $\mathbf{H}_{\text{ext}}$ is in the $Y-Z$ plane and at a rotatable angle θ relative to the Z-directed sample normal. The static magnetization $\mathbf{M}_s$ is also in the $Y-Z$ plane and at a rotatable angle ϕ relative to Z.

perpendicular to the microwave field and the magnet was rotated to move the static field from out of plane to in plane. All measurements were made at 9.5 GHz.

A schematic diagram of the spectrometer system is shown in Fig. 3. The continuous wave microwave signal was generated by a synthesized microwave source and transmitted through an isolator to a shorted TE_{10} waveguide section in the gap of the electromagnet. The circular film sample was positioned on the side of the waveguide section as shown, and the adjustable short was used to maximize the amplitude of the microwave field at the sample position. The reflected power was monitored through a 3 dB directional coupler and a crystal detector. Response curves of the derivative of the FMR absorption were obtained with a conventional lock-in amplifier and field modulation techniques. The modulation field amplitude was on the order of 5 Oe or smaller, and always kept well below the FMR linewidth for the specific measurement underway. A personal computer was used for system controller and data acquisition.

The inset in Fig. 3 shows the circular film sample and field geometry. The microwave magnetic field **h** is in the plane of the film and vertical. The static external field $\mathbf{H}_{\text{ext}}$ is in the horizontal plane and at an angle θ to the film normal. This field angle can be changed from out of plane to in plane through the rotation of the magnet. The inset also shows the magnetization vector $\mathbf{M}_s$ in the horizontal plane and at an angle ϕ to the film normal. The geometry shown in the inset will be important for the analysis of Sec. IV.

For the measurements considered below, the external field angle was varied from out of plane to in plane in steps of approximately 2°. At each angle, curves of the derivative of the FMR absorption were recorded. The FMR field at the center of the absorption line and the derivative linewidth, taken as the separation in field between the extrema of the FMR derivative curve, were obtained. The results given below will be in terms of half-power linewidths, which are a factor of $\sqrt{3}$ greater than the derivative linewidth for an assumed Lorentzian line shape.

IV. THEORETICAL CONSIDERATIONS

A. Uniform mode analysis

The sample geometry was described above and shown in the Fig. 3 inset. The diagram applies to a uniformly magnetized isotropic thin film with no significant anisotropy. As shown in the inset, the magnetization angle ϕ is greater than the field angle θ. In the limit of a small or zero field, $\mathbf{M}_s$ would move to the in-plane direction along the Y axis. In the limit of a very large field, $\mathbf{M}_s$ would rotate into near alignment with $\mathbf{H}_{\text{ext}}$. Simple torque considerations yield the following condition for static equilibrium:

$$4H_{\text{ext}}\sin(\phi-\theta)=[4\pi M_s(3N_Z-1)]\sin(2\phi). \tag{1}$$

For a given field angle θ, Eq. (1) has ϕ solutions which range from $\phi\gtrsim\theta$ for very large fields to $\phi\approx 0$ for small fields. For the perpendicular field case, $\theta\rightarrow 0°$, the ϕ solution also goes to 0°. For the parallel field case, $\theta\rightarrow 90°$, the ϕ solution goes to 90° as well.

Turn now to the uniform mode response. The microwave field **h** is along the X direction and of the form $he^{i\omega t}$, where h is the field amplitude and ω is the microwave frequency. The magnetization vector $\mathbf{M}(t)$ is taken to consist of the static component $\mathbf{M}_s$ in the Fig. 3 inset and a small dynamic component $\mathbf{m}e^{i\omega t}$. In the small signal limit, one may neglect the component of **m** which is parallel to $\mathbf{M}_s$, write the total time dependent magnetization vector as

$$\mathbf{M}(t)=\mathbf{M}_s+\mathbf{m}_\perp e^{i\omega t}, \tag{2}$$

and then use the torque equation of motion with an appropriate damping term to describe the response of the transverse dynamic magnetization $\mathbf{m}_\perp$. If a damping term of the Landau–Lifshitz form is assumed, this equation of motion may be written as

$$\frac{d\mathbf{m}_\perp(t)}{dt}=-|\gamma|[\mathbf{M}(t)\mathbf{H}(t)]-\lambda\frac{\mathbf{M}(t)}{M_s^2}[\mathbf{M}(t)\mathbf{H}(t)]. \tag{3}$$

In Eq. (3), γ is the electron gyromagnetic ratio and λ is the LL relaxation rate. The field $\mathbf{H}(t)$ represents the total effective field in the sample and includes the static external field $\mathbf{H}_{\text{ext}}$, the applied microwave field **h**, static demagnetizing fields associated with $\mathbf{M}_s$, and dynamic demagnetizing fields associated with $\mathbf{m}_\perp$.

One then retains in Eq. (3) only linear terms in the components of $\mathbf{m}_\perp$ and **h**, and solves for the complex $\mathbf{m}_\perp$ response. For the geometry of Fig. 3, the negative imaginary part of the X component of $\mathbf{m}_\perp$ corresponds to the ferromagnetic resonance power absorption or loss. Considered as a function of frequency ω at fixed H_{ext} and fixed field angle θ, this loss profile typically has the form of a peaked Lorentzian function. This profile has two important parameters, the frequency position of the peak and the width of the Lorentzian.

The peak position is the FMR frequency $\omega_{\rm FMR}$ and the full width at half maximum for the Lorentzian is the half power frequency linewidth $\Delta\omega$.

Apart from a small correction due to the damping, $\omega_{\rm FMR}$ and the LL frequency linewidth $\Delta\omega_{\rm LL}$ are given by

$$\omega_{\rm FMR}=|\gamma|\sqrt{H_X H_{YZ}} \tag{4}$$

and

$$\Delta\omega_{\rm LL}=\frac{\lambda}{M_s}(H_X+H_{YZ}). \tag{5}$$

The H_X and H_{YZ} terms in Eqs. (4) and (5) represent effective stiffness fields associated with the tipping of the magnetization vector $\mathbf{M}_s$ away from its equilibrium position in Fig. 3 toward either the X axis or in the transverse $Y-Z$ plane, respectively. These stiffness fields are given by

$$H_X=H_{\rm ext}\cos(\phi-\theta)-\frac{1}{2}[4\pi M_s(3N_Z-1)]\cos^2\phi, \tag{6}$$

and

$$H_{YZ}=H_{\rm ext}\cos(\phi-\theta)-\frac{1}{2}[4\pi M_s(3N_Z-1)]\cos(2\phi). \tag{7}$$

Keep in mind that the field angle θ and magnetization angle ϕ are related through Eq. (1). For a given value of $H_{\rm ext}$, both $\omega_{\rm FMR}$ and $\Delta\omega$ will be θ dependent.

In the parallel and perpendicular FMR limits, the above equations reduce to expressions connecting $\omega_{\rm FMR}$ and $H_{\rm ext}$

$$\omega_{\rm FMR}(\text{parallel})=|\gamma|\sqrt{H_{\rm ext}(H_{\rm ext}+4\pi M_s)}. \tag{8}$$

$$\omega_{\rm FMR}(\text{perpendicular})=|\gamma|(H_{\rm ext}-4\pi M_s). \tag{9}$$

Typical FMR measurements, including those reported here, are done at fixed frequency rather than fixed field. In order to obtain the FMR field $H_{\rm FMR}$ for a given field angle θ and given operating point frequency ω, one sets $\omega_{\rm FMR}$ in Eq. (4) equal to ω and then solves Eqs. (1), (4), (6), and (7) for the values of $H_{\rm ext}$ and ϕ which satisfy the FMR condition of Eq. (4). Such evaluations may be used to check the experimental validity of the uniform mode model. One easy way to do such a check is to use the measured parallel and perpendicular FMR fields and Eqs. (8) and (9) to determine $|\gamma|$ and $4\pi M_s$. These determinations are then used to evaluate $H_{\rm FMR}$ versus θ for comparison with the full ensemble of data on the FMR field versus angle. Some representative results of this procedure and a tabulation of the applicable $|\gamma|$ and $4\pi M_s$ values for the YIG, MnZn ferrite, and NiZn ferrite films will be given in Sec. V A. These results will be seen to support the uniform mode model quite well.

Turn now to the analysis of linewidths. Equation (5) gives the Landau–Lifshitz frequency linewidth for FMR at fixed field. The simplest way to obtain the field linewidth $\Delta H_{\rm LL}$ for fixed frequency FMR at a given field angle θ is to evaluate the change in $H_{\rm FMR}$ with ω at the chosen operating frequency, and apply the approximation

$$\Delta H_{\rm LL}\approx\frac{\partial H_{\rm FMR}}{\partial\omega}\Delta\omega_{\rm LL}. \tag{10}$$

Alternatively, one may evaluate the FMR loss profile versus field and determine the half-power field linewidth numerically. The results to be presented in Sec. V will be based on numerical evaluations.

Note that in the perpendicular resonance limit for which Eq. (9) applies, the derivative term in Eq. (10) is simply equal to $1/|\gamma|$. In this case, the field linewidth $\Delta H_{\rm LL}$ and frequency linewidth in field units, $\Delta\omega_{\rm LL}/|\gamma|$, are equal. In general, however, these linewidths will be different. Since $\Delta\omega_{\rm LL}$ will be a function of the field angle θ through the angle dependence of the H_X and H_{YZ} terms in Eq. (5), $\Delta H_{\rm LL}$ will be θ dependent as well. The LL field linewidth, moreover, will have an additional angle dependence derived through the θ-dependent term in Eq. (10).

How may this LL linewidth analysis be applied to the data on linewidth versus angle and two magnon scattering? The procedure for the data analysis of Sec. V was as follows: (i) Based on the materials parameters obtained from the fits of $H_{\rm FMR}$ versus θ to the data, and some working value of the LL relaxation rate λ, one evaluates $\Delta H_{\rm LL}$ versus θ. (ii) One then adjusts this working value of λ so that the $\Delta H_{\rm LL}$ versus θ profile comes up to but does not exceed the measured linewidths for any θ value. (iii) The difference between the measured linewidth ΔH and $\Delta H_{\rm LL}$, taken as a function of angle, is then used as a starting point for the two magnon analysis. For comparisons with two magnon predictions, and as in Refs. 17 and 18, the linewidth difference from (iii), $\Delta H-\Delta H_{\rm LL}$, is converted back to a frequency linewidth based on Eq. (10). The reasons for this second conversion will be apparent from the discussion of two magnon scattering to follow.

B. Two magnon linewidth

The two magnon scattering analysis is summarized below. This summary is based on the theory by Sparks, Loudon, and Kittel (SLK)[11] and the recent extension of this theory to anisotropic thin films by Hurben and Patton.[18] No anisotropy effects are considered here, however.

In the two magnon scattering process, a uniform mode spin wave is annihilated and a spin wave with nonzero wave vector is created. In the SLK approach, the inhomogeneities which give rise to the scattering are modeled as empty spherical regions, or pores, in an otherwise uniformly magnetized sample of infinite extent. The pore, in combination with the uniform magnetization in the material, produces the usual dipolar field. The precessing magnetization associated with the uniform mode FMR response causes this dipole field to precess. This dynamic dipole field then couples the uniform mode to degenerate spin waves and provides additional channels for the relaxation. In this two magnon process, the uniform mode FMR response at the pump frequency ω is coupled to spin waves at the same frequency. One major point of emphasis is that the scattering is to degenerate spin waves. This leads to the density of states considerations and the angle dependent linewidths discussed in Sec. II.

From physical considerations, it is clear that the coupling will be large only when the spin wave wavelength is

greater than the pore diameter, or for a spin wave number k which is smaller than π/R, where R is the pore radius. In the SLK analysis, the coupling is also shown to depend on the angle θ_k between the spin wave vector $\mathbf{k}$ relative to the direction of the magnetization vector $\mathbf{M}_s$. These dependences will appear in the θ_k term of Eq. (11), to be considered shortly.

Real materials with real microstructures will have pores, pits, second phase regions, and other inhomogeneities which are far from the simple spherical pore model in the SLK analysis. In order to account for this situation, one may simply average over the angle dependence factors in the SLK model. For the modeling results to be given in Sec. V B, two cases will be considered. (i) When the full SLK formalism is used, the mechanism will be termed ''*spherical void scattering*.'' (ii) When the angle factors are averaged, the mechanism will be termed ''*isotropic scattering*.''

The SLK analysis yields explicit expressions for the rate at which the energy is coupled from the uniform ferromagnetic resonance mode into degenerate spin waves. That is, the sample is pumped at a frequency ω, is in a magnetic field $\mathbf{H}_{\text{ext}}$ which satisfies the FMR condition $\omega_{\text{FMR}}=\omega$, and has a two magnon scattering contribution to the relaxation rate due to the coupling to degenerate spin waves at $\omega_k=\omega$ based on the spherical pore analysis summarized above.

The corresponding frequency linewidth due to two magnon scattering in an isotropic thin film may be written as

$$\frac{\Delta\omega_{\text{TM}}}{|\gamma|}=\frac{3p(4\pi M_s)^2R^3}{(\Delta\omega_k/|\gamma|)}\int_0^{\infty}\int_{a(k)}^{b(k)}(3\cos^2\theta_k-1)^2 \times\left[\frac{j_1(kR)}{kR}\right]^2 d(\cos\theta_k)k^2dk. \tag{11}$$

The notation in Eq. (11) closely follows Ref. 18. The frequency linewidth $\Delta\omega_{\text{TM}}$ divided by $|\gamma|$ gives the two magnon linewidth in field units. The dimensionless parameter p denotes the volume fraction or fractional sample volume for the pores. The parameter $\Delta\omega_k$ denotes the intrinsic frequency linewidth of the spin waves and $\Delta\omega_k/|\gamma|$ expresses this linewidth in field units. This spin wave linewidth is typically 1 Oe or less. It is used here to give a nonzero but small width for the band of degenerate spin waves for the numerical evaluations. The value of $\Delta\omega_k$, as long as it is small relative to the scale of the spin wave band, has no practical effect on the two magnon results.

The double integral over $\cos\theta_k$ from $a(k)$ to $b(k)$ and over wave number k from zero to infinity serves to sum up the scattering contributions from the available degenerate states for a given $\mathbf{H}_{\text{ext}}$. This integral, for example, covers the band of states depicted in each of the diagrams of Fig. 1. The $a(k)$ and $b(k)$ functions give the values of $\cos\theta_k$ at the bottom and top, respectively, of the band of degenerate states at some specific k value in the diagrams of Fig. 1. Cutoffs in the two magnon scattering linewidth contribution when there are no degenerate states may be taken into account by writing the $a(k)$ and $b(k)$ according to the algorithm given below.

$$\begin{matrix}a(k)\\ b(k)\end{matrix}=\begin{cases}1, & \omega\pm\dfrac{\Delta\omega_k}{2}<\omega_{\min}\\ \sqrt{\dfrac{\omega_{\max}^2-\left(\omega\pm\dfrac{\Delta\omega_k}{2}\right)^2}{\omega_{\max}^2-\omega_{\min}^2}}, & \omega_{\min}<\omega\pm\dfrac{\Delta\omega_k}{2}<\omega_{\max}\\ 0, & \omega\pm\dfrac{\Delta\omega_k}{2}>\omega_{\max}\end{cases}. \tag{12}$$

The $\pm$ signs in Eq. (12) apply to $a(k)$ and $b(k)$, respectively. The frequencies $\omega_{\min}$ and $\omega_{\max}$ represent the spin wave frequency at the bottom and top of the spin wave band, respectively. The above expressions automatically take cutoff values into account. If, for example, one has a k value which is outside the band, ω will fall below both $\omega_{\min}$ and $\omega_{\max}$, both $a(k)$ and $b(k)$ will go to 1, and the $\cos\theta_k$ integral will vanish.

These $\omega_{\min}$ and $\omega_{\max}$ band limits may be obtained from the bulk material dispersion relation for the spin wave frequency ω_k as a function of k and θ_k,

$$\omega_k=|\gamma|\sqrt{(H_i+Dk^2)(H_i+Dk^2+4\pi M_s\sin^2\theta_k)}, \tag{13}$$

where H_i is the static internal field for given values of H_{ext}, the field angle θ, and the magnetization angle ϕ. The D parameter denotes an exchange stiffness constant. For a given k value, the top and bottom of the band spin wave frequencies are given by

$$\omega_{\max}=|\gamma|\sqrt{(H_i+Dk^2)(H_i+Dk^2+4\pi M_s)} \tag{14}$$

and

$$\omega_{\min}=|\gamma|(H_i+Dk^2). \tag{15}$$

The internal field H_i in Eqs. (13)–(15) is given by

$$H_i=H_{\text{ext}}\cos(\theta-\phi)-2\pi M_s[\sin^2\phi+N_Z(3\cos^2\phi-1)]. \tag{16}$$

The above equations provide a working basis for the evaluation of frequency linewidths due to two magnon scattering in ferrite films with noninteracting spherical pores of radius R and volume fraction p. The present model is based on the spin wave dispersion for bulk ferrites, as given in Eq. (13) without modification for the thin film geometry. The $(3\cos^2\theta_k-1)^2$ factor in the integrand of Eq. (11) corresponds to spherical void scattering. For calculations in the isotropic scattering limit, the solid angle average of 4/5 for this factor will be used.

For both scattering limits, the k-dependent $j_1(kR)/kR$ factor in Eq. (11) will be retained. This term provides a mathematical cutoff in the scattering for k values greater than π/R. Recall that all the films were on the order of 1 μm thick and optically dense. This means that whatever pores are present will be well below 1 μm in size. Submicron size pores, moreover, place the cut-off k value for two magnon scattering, $k_{\text{cut}}\approx\pi/R$, in the $1-10\times10^5$ rad/cm range. This k_{cut} range is right in the middle of the band of degenerate

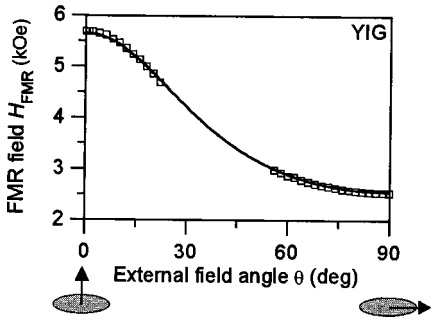

FIG. 4. FMR field H_{FMR} as a function of the external field angle θ for the PLD YIG sample at 9.5 GHz. The open square symbols show the data. The solid curve shows the calculated FMR field based on the uniform mode model.

spin waves depicted in Fig. 1(c). This means that the details of the microstructure can be critical to the angle dependence of the two magnon linewidth. Such effects will be evident both from the data and the computed two magnon linewidth results in Sec. V.

How may the calculated two magnon linewidth versus angle be compared with the data? As indicated above, the experimental parameter which corresponds to the two magnon linewidth in Eq. (11), $\Delta\omega_{\mathrm{TM}}/|\gamma|$, will be the difference between the measured linewidth ΔH and the calculated Landau–Lifshitz linewidth ΔH_{LL} after conversion to an equivalent frequency linewidth. This conversion follows the same procedure given in Eq. (10). The resulting experimental linewidth parameter with possible two magnon origins may be written as

$$\frac{\Delta\omega}{|\gamma|}_{\mathrm{DIFF}} = \frac{\Delta H - \Delta H_{\mathrm{LL}}}{[\partial H/\partial(\omega/|\gamma|)]}. \tag{17}$$

As will be evident from Sec. V B, the angle dependent $\Delta\omega/|\gamma|_{\mathrm{DIFF}}$ extractions show reasonable correlations with the predictions from the two magnon model.

V. RESULTS

A. FMR field versus angle

Figure 4 shows representative results on the ferromagnetic resonance field H_{FMR} as a function of the external field angle θ for fixed frequency FMR at 9.5 GHz. The results shown are for the YIG film. Similar results were obtained for the MnZn and NiZn ferrite films. The open squares show the measurements. The solid curve shows the calculated FMR position versus angle based on the uniform mode model. There are no data for angles between about 20° and 50°. Over this range of angles, the FMR response consists of a complicated multipeaked magnetostatic mode spectra for which no single well defined FMR position is evident.[25]

The solid curve was obtained from the procedure given below Eqs. (8) and (9). First, $4\pi M_s$ and $|\gamma|$ for YIG were obtained from the measured perpendicular and parallel FMR field positions. With these parameters, H_{FMR} versus θ was then evaluated. The calculated FMR field versus angle curve in Fig. 4 matches the data extremely well. This agreement indicates the validity of the uniform mode FMR model.

TABLE I. Empirical values of the saturation induction $4\pi M_s$ and $|\gamma|$ from vibrating sample magnetometer (VSM) measurements and ferromagnetic resonance (FMR).

Film	$4\pi M_s$ (kG) (VSM)	$4\pi M_s$ (kG) (FMR)	$\lvert\gamma\rvert$ (GHz/kOe) (FMR)
YIG	2.21	2.22	2.73
MnZn	3.72	3.80	2.78
NiZn	6.25	6.30	2.97

This same FMR field versus angle measurement and analysis was also done for the MnZn and NiZn ferrite films. These spinel materials had much larger linewidths and the FMR peak positions could be measured over the entire range of angles from perpendicular to parallel. The procedure was the same. The $4\pi M_s$ and $|\gamma|$ values obtained in each case yielded good fits to the data over the full range of angles from perpendicular to parallel.

Table I gives empirical $4\pi M_s$ and $|\gamma|$ values for the YIG, MnZn ferrite, and NiZn ferrite films. Columns 2 and 3 in the table give $4\pi M_s$ values from the VSM measurements and the fits of the FMR data to the uniform mode model, respectively. These $4\pi M_s$ values are in reasonable agreement. Apart from experimental error, the 0.5%–2% differences may be attributed to the experimental uncertainty in the film thickness. The $|\gamma|$ values are all close to the free electron value of 2.8 GHz/kOe. The slightly smaller values for the YIG and MnZn ferrite films, and the larger value for the NiZn ferrite film are consistent with the literature.[21] The $4\pi M_s$ and $|\gamma|$ values from the FMR fits will be used for the two magnon analysis given below.

B. FMR linewidth versus angle

Figures 5, 6, and 7 show the linewidth results for the YIG, MnZn ferrite, and NiZn ferrite films, respectively. The top graph in each figure shows two results. The solid circles and solid lines labeled EXP show measured linewidth versus field angle θ. The lines represent simple fits to the data. The dashed lines labeled INT show calculated intrinsic Landau–Lifshitz linewidth versus θ, based on a constant value of the LL relaxation rate λ. In each case, the value of λ was chosen to put the LL linewidth for perpendicular FMR as close as possible to the measured perpendicular FMR linewidth, while keeping the LL linewidth for all angles below the measured linewidths.

The bottom graph in each figure also shows linewidth versus field angle. These linewidths, however, relate to the two magnon process. Each graph shows three results. The open circles and fitted thin solid lines labeled DIFF show extracted linewidth differences between the data and the LL linewidth results from the top part of the figure. These linewidth differences have been converted to frequency linewidths in accord with Eq. (17) in Sec. IV B. The thick solid lines labeled SLK and ISO in each graph show calculated curves of the two magnon frequency linewidth versus angle based on the SLK and the isotropic scattering models, respectively. Each of the curves was obtained for ''best fit'' choices for the pore radius R and the pore volume fraction p.

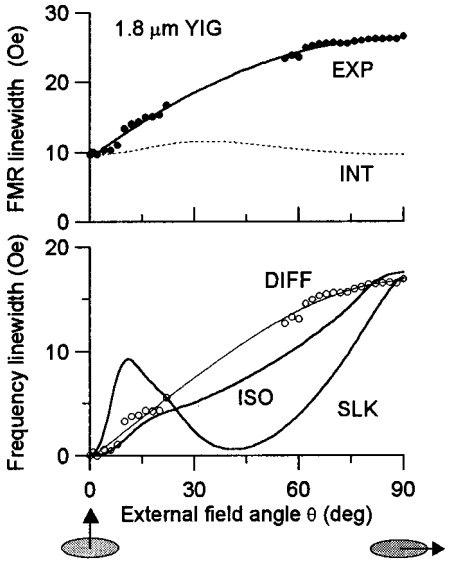

FIG. 5. Linewidth as a function of the external field angle θ for the 1.8 μm PLD YIG film at 9.5 GHz. In the top graph, the solid circles and solid line polynomial fit labeled EXP show the measured FMR linewidth. The dashed line labeled INT shows the calculated LL linewidth for a LL relaxation rate $\lambda = 4.12 \times 10^6$ rad/s. In the bottom graph, the open circles and thin solid line polynomial fit labeled DIFF show the frequency linewidth extractions for the experimental linewidths minus the LL linewidths. The thick solid lines labeled SLK and ISO show two magnon frequency linewidths based on the spherical void SLK and isotropic scattering models, respectively. The SLK and ISO curves were obtained for pore radii of 0.25 and 0.15 μm, and pore volume fractions of 0.1% and 0.16%, respectively.

Consider first the results in the top graphs of the figures. These FMR linewidth versus field angle data show two main results. First, the measured linewidth generally increases as one moves from perpendicular to parallel FMR. Second, the fitted LL linewidth curves indicate a linewidth difference

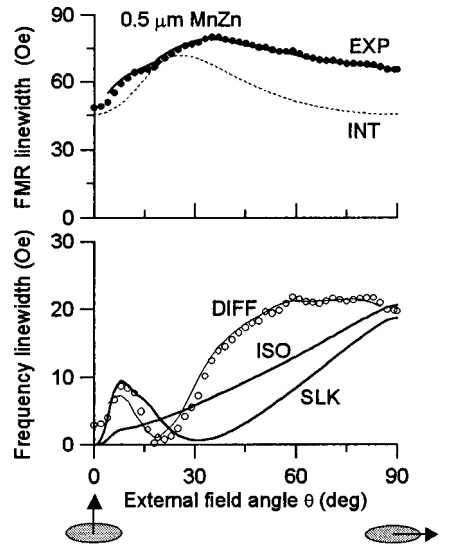

FIG. 6. Linewidth as a function of the external field angle θ for the 0.5 μm PLD MnZn ferrite film at 9.5 GHz. The format and nomenclature are the same as for Fig. 5. The calculated LL linewidth was obtained with a LL relaxation rate $\lambda = 3.57 \times 10^7$ rad/s. The SLK and ISO curves were both obtained for a pore radius of 0.24 μm and a pore volume fraction of 0.06%.

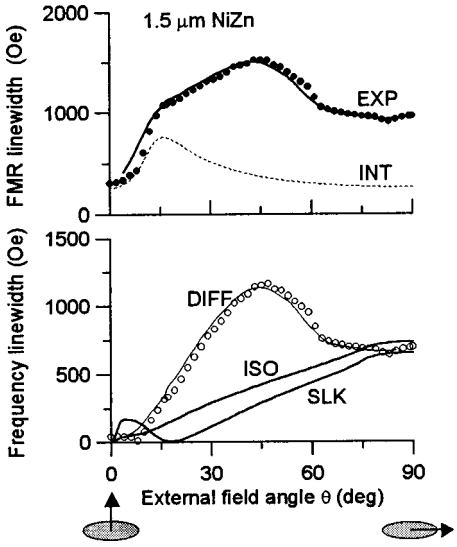

FIG. 7. Linewidth as a function of the external field angle θ for the 1.5 μm PLD NiZn ferrite film at 9.5 GHz. The format and nomenclature are the same as for Fig. 6. The calculated LL linewidth was obtained with a LL relaxation rate $\lambda = 3.83 \times 10^8$ rad/s. The SLK and ISO curves were obtained for a pore radius of 0.3 μm and for pore volume fractions of 0.6% and 0.7%, respectively.

which also increases as one moves from perpendicular to parallel. Both trends support the two magnon hypothesis.

The two magnon linewidth results in the bottom graphs also show that a two magnon mechanism can explain the trend of the data for reasonable choices of the pore radius and pore volume fractions. The R values range from 0.15 to 0.3 μm and the p values range from 0.06% to 0.7%. These values are consistent with the scanning electron micrograph data of Dorsey *et al.*,[8] which indicate submicron R values and dense PLD films. The fact that such a range of parameters can produce two magnon linewidths on the same scale as the data is an important conclusion for this work.

Apart from the agreement of scale, however, the calculated two magnon linewidth versus angle curves in Figs. 5–7 do not give a quantitative match with the extracted linewidth difference data for either the SLK or the isotropic scattering model. Some aspects of the fits appear to follow the trend of the data and some do not. These details are best considered on a case by case basis.

The isotropic scattering fit in Fig. 5 for the YIG comes closest to a quantitative match to experiment. The isotropic scattering curve (i) shows a good match to the end point data at parallel FMR, (ii) follows the initial increase in the linewidth difference from the perpendicular end point up to about $\theta \approx 15° - 20°$, and (iii) falls somewhat below the data for the middle angles by only about 30%. This fall off from the data for the theoretical ISO curve beginning at $\theta \approx 15° - 20°$ can be attributed to a cutoff in the scattering efficiency for high k spin waves due to the relatively large pore radius.[18] As discussed in Sec. IV B, submicron size pores put the cut-off k value for scattering right in the middle of the degenerate state region. The fact that the data show no such change may indicate that the cutoff in scattering occurs much more gradually than the single pore model predicts. It is clear, nevertheless, that isotropic scattering, for which the

spin wave angle factor $(3\cos^2\theta_k-1)^2$ term of Eq. (11) is replaced by its average value over all solid angles, provides near quantitative agreement between theory and experiment for reasonable values of R and p. None of the strong angle dependences observed in the SLK curve are evident in the data.

It is important to emphasize that the linewidth difference data in all of the bottom graphs depends critically on the choice of the LL relaxation rate λ and the resulting position of the LL linewidth versus angle INT curve in the top graphs. For YIG, it was possible to adjust λ to match the intrinsic linewidth to the measured linewidth at perpendicular FMR and achieve a linewidth difference which increases with angle in a more-or-less smooth fashion. This smooth response closely matches the two magnon ISO response curve.

The MnZn and NiZn results in Figs. 6 and 7 provide a stark contrast to the YIG results. Here, the measured linewidths (i) are larger than for the YIG films and (ii) show broad peaks and more structure as a function of the field angle. The scales of the YIG, MnZn, and NiZn linewidth data are 30, 90, and 2000 Oe, respectively. The angle profiles for the MnZn and NiZn data, moreover, are completely different than the YIG profiles. Here, the linewidths first increase from the values at perpendicular FMR to peak values which are 65% and 400% higher, respectively. These linewidths then decrease to values at parallel FMR which are about 50% and 200% higher than at perpendicular FMR.

The calculated intrinsic linewidth curves in the top graphs of Figs. 6 and 7 are also very different than for YIG. The larger magnetizations for these materials result in Landau–Lifshitz linewidth versus angle profiles which show significant peaks. For the MnZn and the NiZn films, these peaks are about 50% and 200% higher than the end point linewidths, respectively. For YIG, the LL peak was broad and less than 20% of the base linewidth at perpendicular and parallel. The presence of these pronounced LL linewidth peaks present problems in the selection of suitable values of λ to properly position the INT curve and then extract a linewidth difference for the two magnon comparisons.

Focus for the moment on the MnZn results in Fig. 6. If λ is chosen to fit the end point experimental linewidth value at perpendicular FMR, then the LL linewidth at the peak will be slightly higher than the measured linewidth. Insofar as the LL linewidth is taken here to represent the intrinsic linewidth, it is unreasonable for this peak LL linewidth point to be above the data. The only reasonable choice is to adjust the LL relaxation rate parameter to a somewhat smaller value so that the INT linewidth curve just touches the data. This situation is shown in the top graph of Fig. 6.

This procedure leads to a linewidth difference versus angle response with significant structure. The fact that the INT curve has been adjusted to just touch the EXP results, in combination with the contact point at $\theta\approx 20°-25°$, leads to the double peaked linewidth difference response shown by the open circle data points and the fitted curve in the bottom graph. The small closed pocket between the INT curve and the EXP results for $\theta=0°-20°$ gives the smaller peak in the bottom graph, and the large open pocket for $\theta=25°-90°$ gives the larger peak.

Turn now to the theoretical responses shown in the bottom graph of Fig. 6. Both the SLK and the ISO curves have shapes similar to those shown in Fig. 5. Both responses initially increase from zero as one moves away from perpendicular FMR. The ISO curve shows a smoothly increasing two magnon linewidth which simply reflects the increase in the number of available spin wave states for scattering. The SLK curve goes through a small maximum at $\theta\approx 7°-8°$, drops to minimum at $\theta\approx 30°-32°$, and then increases to a sizable maximum at parallel FMR. The strong angle dependence for the SLK response reflects both the change in the density of states with angle and the strong θ_k dependence for the scattering which comes from the $(3\cos^2\theta_k-1)^2$ term in Eq. (11).

It is important to note that the exchange stiffness parameter D for the two magnon evaluations in Fig. 6 (and Fig. 7) was set at a value of 7×10^{-9} Oe cm^2/rad^2, compared to the nominal YIG value of 5×10^{-9} Oe cm^2/rad^2. The examination of two magnon linewidth versus angle profiles for various D, R, and p values indicate that the proper choice of D is extremely critical. The interplay of these parameters and their effect on the linewidth is discussed in detail in Ref. 18. In the present application, the use of $D=7\times10^{-9}$ Oe cm^2/rad^2 yields two magnon linewidth profiles which scale with the data for values of R and p which are consistent with Ref. 8. If D is reduced to the YIG value, a seemingly small change, an increase in p to several percent is needed to match the scale of the data.

Notwithstanding the rather *ad hoc* procedure which was used to obtain first the INT curve in the top graph of Fig. 6, and then the peaked results for the linewidth difference data in the bottom graph, the low angle SLK peak from the model appears to match the low angle linewidth difference peak from the data rather well. As one moves to larger angles, however, the SLK curve does not follow well the second rise in linewidth shown by the data. The SLK curve goes to a minimum at $\theta\approx 30°-32°$ and then increases gradually to a maximum at 90°. The experimental minimum is at $\theta\approx 20°-25°$ and the data rise to a broad maximum for larger angles.

Apart from the problems with the shifted minimum and the broad second peak at large angles, it appears that the spherical pore scattering model is qualitatively consistent with the MnZn data. At the same time, it is clear that distributions in pore size and shape, and the other complications associated with the real microstructure, shifts the measured angle dependence from the simple model predictions in a significant way. The results in Fig. 6 are similar to results for two magnon scattering in dense polycrystalline YIG spheres.[26]

The ISO curve in Fig. 6 provides no quantitative matchup whatsoever with the low angle peak from the data. Apart from the small kink at about 7°–8° associated with the cutoff in scattering for $k>\pi/R$, discussed above, the ISO two magnon linewidth response increases smoothly from perpendicular to parallel. Isotropic scattering, therefore, does

not appear to be operative for the MnZn film, even though it is the dominant process for YIG.

The above discussion aside, it is important to emphasize again that the angle dependences shown for the experimental DIFF curve in Fig. 6 derive from the LL fit procedure and the linewidth pockets which result from that fit. Without these pockets, the low angle peak which appears in the DIFF curve in Fig. 6 would become much less prominent, and the difference linewidth versus angle profile would be more like the calculated ISO response.

Finally, turn to the NiZn ferrite results in Fig. 7. The linewidth data show a completely different character from the YIG and MnZn data. First, the linewidths here are much larger, more than 50 times greater than the YIG linewidths and more than 20 times greater than the MnZn linewidths. Second, the linewidth versus angle profile shows a broad peak, as for the MnZn case, but the profile also shows considerably more structure. Third, the larger linewidths and, in particular, the rapid increase in the linewidth as one moves away from perpendicular FMR, make it possible to perform a reasonable LL fit without producing the pockets found for the MnZn analysis. Note that these pockets are avoided even though the LL peak linewidth is about twice the perpendicular linewidth, compared to the roughly 50% increase for the MnZn.

These characteristics lead to the broad peaked DIFF linewidth profile shown in the bottom part of Fig. 7. As the fits show, neither the SLK or the ISO model can provide a match to this broad peak. As for the YIG and MnZn cases, reasonable values of R and p do produce calculated response curves which match the end point DIFF data at parallel FMR reasonably well. Note, however, that the p value needed to obtain the large linewidths here is a factor of 10 greater than the fitted p value for the MnZn.

What basic conclusions concerning the FMR linewidth in PLD films, intrinsic losses, two magnon scattering, and microstructure can be drawn from the above results? As emphasized above, the YIG films provide the best connections. For the PLD YIG, the intrinsic linewidth at X band is about 10 Oe, still a factor of 20–25 or so above the lowest room temperature linewidths in single crystal YIG bulk[27] and liquid phase epitaxy film[28] materials. The additional linewidth increases, more-or-less smoothly as one moves from perpendicular to parallel FMR, and this increase can be modeled in terms of isotropic scattering with submicron pore sizes and volume fractions of 0.1%.

A two magnon analysis for the MnZn and NiZn PLD films is problematic at best. First, the intrinsic linewidths are much larger, on the order of 45 Oe for the MnZn and 300 Oe for the NiZn. Second, the relatively large magnetizations result in a pronounced peak in the computed LL linewidth which complicates the extraction of a reliable linewidth difference for use in the two magnon analysis. In the MnZn case, the most reasonable choice for the LL fit produces a linewidth difference with pockets, a small one at low angles and a large one at large angles. The small angle pocket provides an apparent match with the two magnon linewidth peak predicted at small angles for SLK scattering. The large angle pocket produces a broad peak in the linewidth difference which appears to be inconsistent with a two magnon process. For the NiZn case, the small pocket is not found and the broad peaked pocket is accentuated. On the positive side, the scale of the observed linewidth increase with angle is consistent with the computed two magnon losses for submicron pore sizes and volume fractions below 1%.

VI. SUMMARY AND CONCLUSION

This work concerns microwave losses in pulsed laser deposited thin films of YIG, MnZn, and NiZn. Shorted waveguide ferromagnetic resonance measurements were made at a fixed frequency of 9.5 GHz. The FMR field and linewidth were measured as a function of the external field angle with the film normal. The data were analyzed in terms of the uniform mode FMR model, intrinsic Landau–Lifshitz relaxation, and two magnon scattering. Computed curves of the LL linewidth versus angle were fitted to the linewidth data and used to extract a linewidth difference for analysis in terms of two magnon scattering.

The extracted linewidth difference data provide qualitative support for a two magnon contribution to the FMR linewidth for PLD films. Especially good agreement was obtained for the YIG film. Here, the LL linewidth was about 10 Oe, the two magnon linewidth increased smoothly from 0 at perpendicular FMR to about 20 Oe, and the increase could be modeled with isotropic two magnon scattering from 0.15 μm pores with a small volume fraction of 0.16%. The MnZn and NiZn data showed a linewidth increase from perpendicular to parallel which is qualitatively consistent with two magnon scattering, submicron pore sizes, and pore volume fractions below 1%. Apart from a small low angle peak in the extracted linewidth difference for the MnZn film which appears to agree with SLK scattering, the spinel ferrite film data could not be reconciled with a quantitative two magnon model. Of particular concern is a broad maximum in the extracted linewidth difference which is not found in the two magnon analysis.

Where do these results lead? First, it is clear that the microwave losses in PLD ferrite films produced to date are far from intrinsic. The linewidth for perpendicular FMR, which should contain no two magnon scattering contribution, is well above the lowest linewidths found for the same materials in bulk single crystal form. Second, it is also clear that the angle dependence of the measured linewidths indicate the presence of additional mechanisms for linebroadening, over and above whatever mechanisms are responsible for the intrinsic losses. Further work is needed to (i) reduce the intrinsic linewidth in PLD films and (ii) understand quantitatively the role of microstructure in producing the additional linewidth which is found experimentally.

ACKNOWLEDGMENTS

The authors acknowledge Professor Boris A. Kalinikos of the St. Petersburg Electrotechnical University, St. Petersburg, Russia, Richard G. Cox, and Dr. Christoph Mathieu of Colorado State University for helpful discussions during the course of this work. Dr. Mathieu also provided a careful reading of the final manuscript. This work was supported by

the United States Office of Naval Research. The measurements and analysis at Colorado State University were supported by the Grant No. N00014-94-1-10096. The materials development at the University of Maryland was supported by the Grant No. N00014-95-1-0547. The materials development at the Naval Research Laboratory was supported by the Grant No. N00014-94-AF-0002.

[1] G. K. Hubler, MRS Bull. **17**, 26 (1992).
[2] C. J. Yang, S. W. Kim, and Y. S. Kim, IEEE Trans. Magn. **30**, 4527 (1994).
[3] H. Buhay, J. D. Adam, M. R. Daniel, N. J. Doyle, M. C. Driver, G. W. Eldridge, M. H. Hanes, R. L. Messham, and M. M. Sopria, IEEE Trans. Magn. **31**, 3832 (1995).
[4] F. J. Cadieu, R. Rani, W. Mendoza, B. Peng, S. A. Shaheen, M. J. Hurben, and C. E. Patton, J. Appl. Phys. **81**, 4801 (1997).
[5] S. A. Oliver, C. Vittoria, G. Balestrino, S. Martellucci, G. Petrocelli, A. Tebano, and P. Paroli, IEEE Trans. Magn. **30**, 4933 (1994).
[6] C. M. Williams, D. B. Chrisey, P. Lubitz, K. S. Grabowski, and C. M. Cotell, J. Appl. Phys. **75**, 1676 (1994).
[7] C. A. Carosella, D. B. Chrisey, P. Lubitz, J. S. Horwitz, P. Dorsey, R. Seed, and C. Vittoria, J. Appl. Phys. **71**, 5107 (1992).
[8] P. C. Dorsey, S. E. Bushnell, R. G. Seed, and C. Vittoria, J. Appl. Phys. **74**, 1242 (1993).
[9] C. R. Buffler, J. Appl. Phys. **30**, 172S (1959).
[10] H. B. Callen, J. Phys. Chem. Solids **4**, 256 (1958).
[11] M. Sparks, R. Loudon, and C. Kittel, Phys. Rev. **122**, 791 (1961).
[12] C. E. Patton, in *Magnetics Oxides*, edited by D. J. Craik (Wiley, London, 1975), Chap. 10.
[13] C. E. Patton, J. Appl. Phys. **38**, 1358 (1967).
[14] C. E. Patton, J. Appl. Phys. **39**, 3060 (1968).
[15] C. E. Patton, AIP Conf. Proc. **10**, 135 (1972).
[16] R. D. McMichael, M. D. Stiles, P. J. Chen, and W. F. Egelhoff, Jr., J. Appl. Phys. **83**, 7037 (1998).
[17] M. J. Hurben, D. R. Franklin, and C. E. Patton, J. Appl. Phys. **81**, 7458 (1997).
[18] M. J. Hurben and C. E. Patton, J. Appl. Phys. **83**, 4344 (1998).
[19] B. M. Simion, R. Ramesh, and G. Thomas, J. Appl. Phys. **79**, 5935 (1996).
[20] J. A. Osborn, Phys. Rev. **67**, 351 (1945).
[21] W. H. von Aulock, *Handbook of Microwave Ferrite Materials* (Academic, New York, 1965).
[22] P. C. Dorsey, P. Lubitz, V. G. Harris, D. B. Chrisey, and J. S. Horwitz, IEEE Trans. Magn. **31**, 3455 (1995).
[23] M. Chen and C. E. Patton, in *Nonlinear Phenomena and Chaos in Magnetic Materials*, edited by P. E. Wigen (World Scientific, Singapore 1992), Chap. 3.
[24] W. D. Wilber, P. Kabos, and C. E. Patton, IEEE Trans. Magn. **MAG-19**, 1862 (1983).
[25] P. E. Wigen, T. S. Stakelon, H. Puszkarski, and P. Yen, AIP Conf. Proc. **29**, 670 (1975).
[26] C. E. Patton, J. Appl. Phys. **40**, 1427 (1969).
[27] E. G. Spenser, R. C. LeCraw, and A. M. Clogston, Phys. Rev. Lett. **3**, 32 (1959).
[28] J. D. Adam, M. R. Daniel, P. R. Emtage, and S. H. Talisa, in *Thin Films for Advanced Electronic Devices*, edited by M. H. Francombe and J. L. Vassen (Academic, Boston, 1991), Vol. 15, p. 1.